Chemistry of Hydrolysis of $FeCl_3$ in the Presence of Phosphate to Form Hematite Nanotubes and Nanorings

Jialu Chen,[†] Shona Macfarlane,[†] Chenxi Zhang,[‡] Kai Yu,[†,§] and Wuzong Zhou[*,†]

[†]EaStCHEM, School of Chemistry, University of St Andrews, St Andrews, Fife KY16 9ST, United Kingdom

[‡]Institute of New Catalytic Materials Science and MOE Key Laboratory of Advanced Energy Materials Chemistry, School of Materials Science and Engineering, National Institute of Advanced Materials, Nankai University, Tianjin 300350, China

[§]MOE Key Laboratory of Pollution Processes and Environmental Criteria, College of Environmental Science and Engineering, Nankai University, Tianjin 300350, China

ABSTRACT: Through investigation of the intermediate specimens during the hydrolysis of $FeCl_3$ in the presence of phosphate using Mass spectroscopy, XRD, EDX, SEM, HRTEM and ICP-OES Spectrometry, the formation mechanisms of α-Fe_2O_3 nanotubes and nanorings were revealed. At early stages, the precursor molecules polymerized and aggregated into large disordered particles, from which β-FeOOH nanorods grew up. When the NaH_2PO_4 concentration was low (*e.g.* 1 mM in a solution of 23 mM $FeCl_3$), the β-FeOOH nanorods were relatively stable and underwent side-by-side aggregation into spindle-like particles. Phase transformation into self-orientated α-Fe_2O_3 nanocrystallites then took place on the surface of these spindle particles, followed by Ostwald ripening, to form a single-crystalline shell. The ends and the core of the spindle particles were dissolved, forming α-Fe_2O_3 nanotubes. When the NaH_2PO_4 concentration was high (*e.g.* 4 mM), the individual β-FeOOH nanorods decomposed into α-Fe_2O_3 nanocrystallites, which underwent self-orientated aggregation into polycrystalline disks. Surface Ostwald ripening and dissolution of the central area turned these disks into nanorings. The exposed surface in the nanotubes is mainly (*hko*), while it is (001) in the nanorings. Photoelectrochemical measurement indicated that photocurrent response of the nanotubes was three times higher than the nanorings. This newly established nonclassical formation mechanisms of these crystals may help us to understand the development of many other novel morphologies of metal oxides via a hydrolysis process.

INTRODUCTION

Hematite (α-Fe_2O_3) has been extensively studied because it is abundant, stable, low-cost, environmentally friendly and it has several interesting properties, such as narrow band gap energy of 2.2 eV, large theoretical specific capacitance (3625 $F \cdot g^{-1}$) and antiferromagnetism.[1–3] These features enable it to be a good candidate for photocatalysts, photoelectrodes, semiconductors, *etc*.[4–6] The properties of α-Fe_2O_3 nanoparticles are highly dependent on its size and morphologies. For example, the different exposed facets of α-Fe_2O_3 can have influence on its performance in photocatalysis.[7] While, synthetic α-Fe_2O_3 nanoparticles can be made in various morphologies, such as nanocubes,[8] nanorods,[9] nanofibres,[10] core-shell nanoplates,[11] *etc*.

According to the classical theory of crystal growth, crystals tend to form a morphology which has a minimum surface energy. To obtain unusual morphologies, three methods are commonly applied. The first is to use a template and the shape of the product is a negative replica of the template.[12] The second is to use restricted growth sites. For example, the growth of silicon nanowires on Au catalytic nanoparticles restricts the diameter of the nanowires by the Au particle size.[13] The third is selective surface adsorption of some molecules to reduce the growth rate on these surfaces. For example, to control the morphology of α-Fe_2O_3 nanoparticles, both inorganic and organic additives are normally used in a hydrothermal process, of which Cl^-, PO_4^{3-}, SO_4^{2-} are common anions used.[14–17] Lv *et al*. synthesized α-Fe_2O_3 nanoparticles with various morphologies by adding sodium phosphate monobasic and studied the formation mechanism.[18] It was proposed that because the adsorption ability of phosphate on the (001) plane of hematite was lower than other planes, the (001) plane was less protected. As a result, the crystal growth along the [001] direction was faster than other directions. It was believed that this was the main reason for the formation of the nanospindle shape of hematite particles, when a single nucleation process was postulated. However, no sufficient experimental data support such a growth mechanism. Our

knowledge of the formation of various morphologies of hematite crystals is still very limited. In fact, formation of many crystal morphologies does not rely on any template and cannot be explained by surface protection. Some non-classical specific crystal growth routes have to be considered.

In our previous studies, snowflake-, feather-, leaf-shaped hematite crystals were produced via hydrolysis of ferricyanide. Highly selective surfaces for attracting precursor $[Fe(CN)_6]^{3-}$ and surface hydrolysis of these anions on α-Fe_2O_3 crystals was found to be a crucial process in the formation of these novel morphologies.[19,20] On the other hand, Liu, *et al*. reported that spindle-, nanotube-, nanodisk-, nanoring-shaped hematite crystals were also synthesized via hydrolysis of $FeCl_3$ in the presence of low or high concentrations of phosphate anions and urea.[21] However, the role of phosphate in the formation of these morphologies was not understood in detail.

In the present work, spindle-, nanotube-, nanodisk-, nanoring-shaped hematite crystals were re-produced using a similar method as previously reported. Some intermediate specimens during the hydrothermal treatment were collected and their compositions and microstructures investigated by using various techniques. New formation mechanisms of the unusual morphologies of hematite are established. The new knowledge allows us to well control the crystal morphology of hematite and its exposed surface, and therefore to tune its physico-chemical properties. Furthermore, this knowledge would also help us to understand non-classical crystal growth routes of many other crystalline materials.

EXPERIMENTAL SECTION

Synthesis of α-Fe_2O_3 nanotubes and nanorings. The synthetic method was similar to that reported by Lv, *et al*.[18] In a typical synthesis, ferric chloride hexahydrate (97%, Alfa Aesar) and sodium phosphate monobasic (99.0%, Sigma) were dissolved in distilled water separately and mixed together into a 40 mL solution. The concentration of $FeCl_3$ was 23.1 mM, while two concentrations of NaH_2PO_4 were used, 1.0 and 4.0 mM, respectively. The solution was transferred to a 50 mL autoclave and heated at a temperature of 220 °C for different times in a range from 30 min to 120 h. After heating, the autoclave was cooled down naturally and the precipitate was centrifuged and washed with distilled water three times. The samples are designated, *e.g*. LS220-xh and HS220-xh, where L and H stand for the low (1.0 mM) and high (4.0 mM) concentrations of NaH_2PO_4, 220 indicates the reaction temperature and xh is reaction time in hours. When slowing down the reaction rate was required, a lower temperature of 180 °C was used and the corresponding specimens are labeled LS180-xh and HS180-xh.

Liu *et al*. reported that using urea to replace phosphate in the system, no spindle particles, nanodisks, nanotubes or nanorings were produced. But adding urea to the phosphate-containing system would enhance the formation of hollow particles.[21] In the present work, two series of samples were prepared using about the same concentrations of phosphate and urea of (1) 1.0 mM and (2) 2.5 mM, while the concentration of $FeCl_3$ remained about the same, 23.0 mM. The reaction temperature was set to 220 °C. The specimens are labeled LU220-xh and HU220-xh, respectively, where U stands for urea. Again, specimens were collected after different reaction times.

The compositions of all the solutions for synthesis with the reaction temperatures are listed in Table 1.

Table 1. The compositions of the solutions (mM) of synthesis and the reaction temperatures (°C).

Label	$FeCl_3$	PO_4^{3-}	Urea	Temp.
LS180	23.1	1.0	0	180
LS220	23.1	1.0	0	220
HS180	23.1	4.0	0	180
HS220	23.1	4.0	0	220
LU220	23.0	1.0	1.0	220
HU220	23.0	2.5	2.5	220

Specimen characterization. Powder X-ray diffraction (XRD) patterns were recorded using a PANalytical Empyrean diffractometer and Cu Kα radiation (λ = 1.5418Å) was the X-ray source. Scanning electron microscopy (SEM) images were recorded using a JEOL JSM-7600F field-emission gun (FEG) electron microscope operating at 5 kV. Samples for SEM were coated with a thin Au layer to overcome the charging problem. Transmission electron microscopy (TEM) and selected area electron diffraction (SAED) patterns were obtained using a JEOL JEM-2011 electron microscope fitted with a LaB_6 electron gun, operating at an accelerating voltage of 200 kV and Titan Themis S/TEM with a FEG, operating at 200 kV. Samples for TEM were prepared by grinding the powder in acetone with a mortar and pestle, and then depositing the sample on a copper grid coated with a holey carbon film. The TEM and high-resolution TEM (HRTEM) images were recorded using a Gatan 794 CCD camera (in JEM-2011) and FEI Ceta 16M CMOS camera (in Titan). The compositions of the particles were examined by using energy dispersive X-ray spectroscopy (EDX) available in all the microscopes.

Mass spectra were obtained using a Thermo Orbitrap mass spectrometer. Samples were prepared by mixing with methanol in the ratio 1:1 and ionized by electrospray. The concentration of Fe^{3+} in the liquid phase was measured using iCAP 6300 ICP-OES Spectrometer. The calibration graph was calculated using 5% HCl solution containing blank, 1 ppm, 5 ppm and 10 ppm Fe^{3+} respectively. The correlation of the calibration graph is 0.999705.

Photoelectrochemical measurement. The photoelectrochemical measurement was carried out on a conventional three-electrode cell by electrochemical workstation (CHI

660D). Two typical samples with different morphologies, nanotube (LS220-48h) and nanoring (HS220-48h), were selected for the test. Typically, 5.0 mg of sample was dispersed in deionized water (190 μL). Then 10 μL of Nafion® 117 solution was added to the above suspension. After ultrasonic treatment for 2 min, the suspension obtained (0.2 mL) was dropped onto the surface of fluorine doped tin oxide (FTO) glass (1.0 × 1.0 cm). The FTO glass with samples was used as the working electrode. The Pt electrode was used as the counter electrode and the Ag/AgCl electrode was used as the reference electrode. The electrolyte was 0.01 M sodium sulfate aqueous solution. The light source was a 300 W Xe lamp equipped with a UV cutoff filter (λ > 420 nm). The current-time (I-t) curves were collected at the open-circuit potential.

RESULTS AND DISCUSSION

α-Fe_2O_3 spindle particles, nanotubes, nanodisks and nanorings have been successfully synthesized. Figure 1 shows low magnification SEM images of these products with a uniform particle size and morphology. XRD patterns from all these samples indicate the same α-Fe_2O_3 structure, rhombohedral with a = 5.05 Å, c = 13.839 Å. One of the XRD patterns from sample LS180-6h, indexed to α-Fe_2O_3, is shown in Supporting Information (SI), Figure S1.

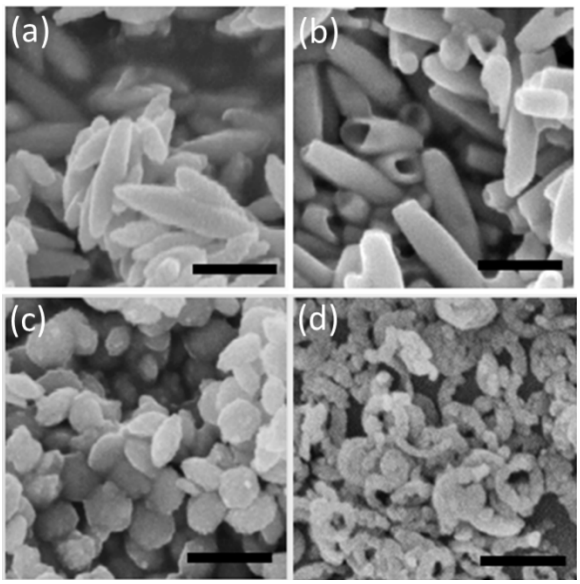

Figure 1. SEM images of hematite particles in (a) LS180-6h showing nanospindle particles; (b) nanotubes in LS220-120h; (c) HS220-3h showing nanodisks; and (d) nanorings in HS220-120h. The scale bar = 300 nm.

Figure 1a shows α-Fe_2O_3 nanospindle particles formed in the low phosphate concentration after reaction at 180 °C for 6 h (*i.e.* sample LS180-6h). With further reaction at higher temperature (220 °C) with longer reaction time (120 h), all the spindle particles changed to nanotubes as seen in Figure 1b. When the concentration of phosphate increased from 1.0 mM to 4.0 mM, α-Fe_2O_3 nanodisks formed in a hydrothermal treatment at 220 °C for 3 h (Figure 1c). The central part of the nanodisks seemed to be dissolved with a longer reaction time (120 h), forming nanorings as shown in Figure 1d.

The variation of temperature from 180 °C to 220 °C did not have a significant influence on the formation of the nanospindle particles and nanodisks. The only difference was that the reaction rate at 180 °C was slightly lower and a longer time was needed to produce similar samples as that formed at 220 °C. On the other hand, the nanotubes and nanorings were not observed from the reaction at 180 °C, implying that partial dissolution, forming nanotubes from the spindle particles or forming nanorings from the nanodisks, requires a higher temperature.

It was also found that addition of urea to the synthetic system did not change the crystal growth route, an enhancement of making hollow particles was not significant. For example, the spindle particles were observed in both specimens of LU220-1h and LS220-1h, and the nanotubes were produced in 24 h in specimens of LU220-24h and LS220-24h (see Figure S2, in SI). Most experimental data used in the discussion were from the synthetic solutions without addition of urea. The hollow property of the nanotubes is revealed by the open ends of the particles as seen in the SEM image (Figure 1b) and further confirmed by TEM image with both a top view and a profile view (see inset of Figure S2b in SI).

To fully understand the formation mechanisms of these hematite nanoparticles, specimens at the different stages of crystal development were collected. Their compositions, crystal phases and microstructures were investigated. The growth of α-Fe_2O_3 nanotubes and nanorings can be described in several distinguishable steps.

Step 1. The precursor molecules polymerized into larger molecules. After hydrothermal treatment for 30 minutes, the solutions of both low and high concentrations of phosphate had changed color from yellow to dark reddish brown, but very little precipitate was observed. Solution specimens were collected for mass spectroscopic study. Some mass spectra in the low mass region are shown in SI, Figure S3. It was found that $FeCl_3$ molecules were not directly dissociated into Fe^{3+} and Cl^-. Some of them underwent polymerization. The Fe-containing molecules detected are monomers $FeCl_3$ and $[FeCl_4]^-$, dimers Fe_2OCl_4, $[Fe_2OCl_5]^-$, Fe_2Cl_6, $[Fe_2Cl_7]^-$, $NaFe_2Cl_7$, $[NaFe_2Cl_8]^-$, and trimers Fe_3Cl_9, and $NaFe_3Cl_{10}$, *etc*. Since chlorine has two stable isotopes, ^{35}Cl and ^{37}Cl, with an approximate ratio of 3 : 1 and the isotopic effect on mass spectra is obvious, the number of chlorine in the molecules can be easily determined.

In the high mass region, there are single peaks at m/z = 1055.9657, 1155.9590, 1255.9515, 1355.9441, *etc*., separated by a gap of m/z = 100 as shown in Figure S4a in SI. Lower and higher m/z with the difference of 100 were also detected. The single peaks indicate that no chlorine or iron is present

and so the structures can only be derived from phosphate. Figure S4b (in SI) shows a typical polymer model proposed, which shows 10 phosphate anions connected to form a long chain molecule, $P(OH)_3H_2O$-O-$[HPO_3]_8$-$P(OH)_3H_2O$ with m/z = 855.7154. The addition of the building unit $P(OH)_3H_2O$ gives rise to an increase of about 100 to the m/z value. The connection of these units to the middle of the chain to create multiple branches without changing the composition is also possible.

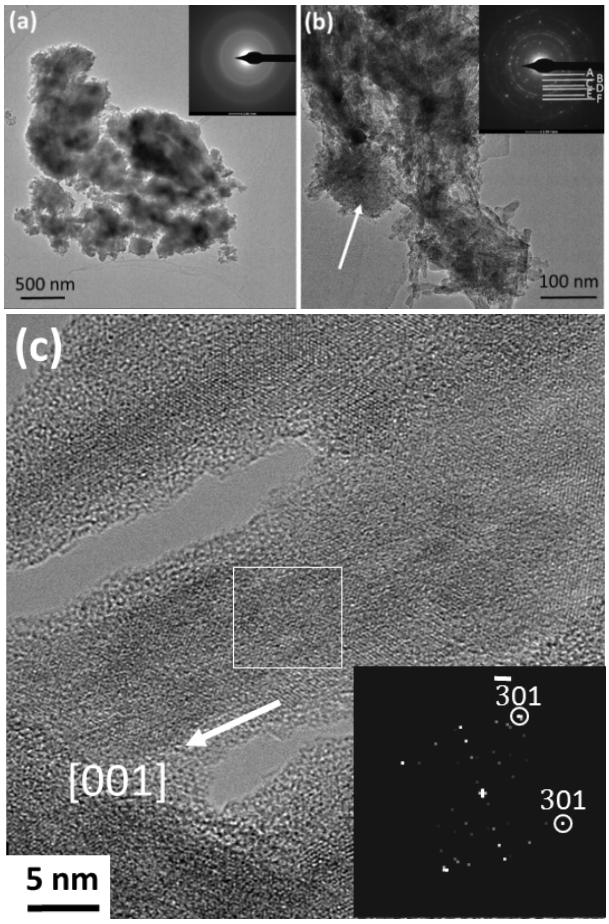

Figure 2. TEM images of (a) LS220-0.5h and (b) HS220-2h. The insets are the corresponding SAED patterns. The pattern in (b) is indexed to tetragonal β-FeOOH structure, A (110), B (200), C (220), D (310), E (211), F (301). The arrow indicates an area of amorphous particle with no nanorods. (c) HRTEM image of LS180-2h which shows individual β-FeOOH nanorods. The inset is the corresponding FFT pattern from an area marked by a square. The pattern is indexed to the β-FeOOH structure.

Step 2. It can be expected naturally that the first precipitate to appear in the solution was mixed Fe-containing molecules and phosphate polymer molecules, which should be non-crystalline irregular particles. This type of particles were occasionally observed from the sample after 30 min reaction (Figure 2a). No nanorods were detected and the particles are amorphous as confirmed by the SAED pattern (inset of Figure 2a). Such aggregates were observed previously, as it was reported that a red cationic polymer forms in ferric chloride solutions and ferric oxide or hydroxide forms from aging of the polymer. The solid polymer contains *ca*. 10^2 ferric ions with a molecular weight of *ca*. 10^4.[22,23] In our own work, EDX of the early stage precipitates showed Fe, O, Cl and P (see Figure S5 in SI), consisting of a possible composition of the aggregates from the Fe-containing molecules and phosphate polymers as mentioned above.

Step 3. Many nanorods soon grew up from the amorphous aggregates. Both SAED patterns and HRTEM images from these nanorods show that they are β-FeOOH crystals with the [001] zone axis parallel to the long axis of the nanorods (Figure 2b, 2c). β-FeOOH as the intermediate phase towards the formation of α-Fe_2O_3 has been discussed in literatures.[24,25] However, this phase was not found previously during the formation of hematite nanotubes and nanorings in a system similar to that used in the present work. The SAED pattern in Figure 2b is indexed to the body-centered tetrahedral structure of β-FeOOH with a = 10.440, and c = 3.010 Å, space group I4/m. In the beginning, the narrow nanorods were embedded in the amorphous matrix and their crystallinity was low (Figure 2c). In further reaction, they grew up into thicker and longer nanorods with high crystallinity, while the thick amorphous surface coating layer observed from Figure 2c disappeared (see Figure S6 in SI).

The most surprising phenomenon was that, after formation of the β-FeOOH nanorods, the crystal growth underwent different processes in low (1.0 mM) and high (2.5 or 4.0 mM) concentrations of phosphate, leading to spindle and nanodisk morphologies, respectively.

β-FeOOH can act as an adsorbent for phosphate anions, due to a strong interaction between phosphate and the hydroxyl groups on the surface of β-FeOOH. Even strong Fe^{3+}-O-P bonds might form via dehydration and phosphate anions are able to bind in a bidentate way, *i.e*. one phosphate anion can bind to two neighboring Fe^{3+} ions.[14,26,27] In the synthetic solution used in this work, the pH was in a range of 1.8 to 1.5, which was lower than the zero point of charge for β-FeOOH (7.2), the surface charge of β-FeOOH was positive and was able to attract monovalent dihydrogen phosphate ions.[28] Due to the fact that the (010) plane of β-FeOOH is the major plane for binding phosphate anions and (001) the minor plane,[27] the geometric shape of the nanorods ensures a side-by-side strong interaction.

Step 4. In the system with 1.0 mM phosphate, the amount of phosphate anions on the β-FeOOH nanorod surface is small. The electrostatic repulsion force between the nanorods is relatively weaker. Therefore, the β-FeOOH nanorods aggregated side-by-side into spindle-shaped particles with a rough surface as shown in Figure 3a. The size of the spindle particles is about 150 nm in diameter and 600 nm in length.

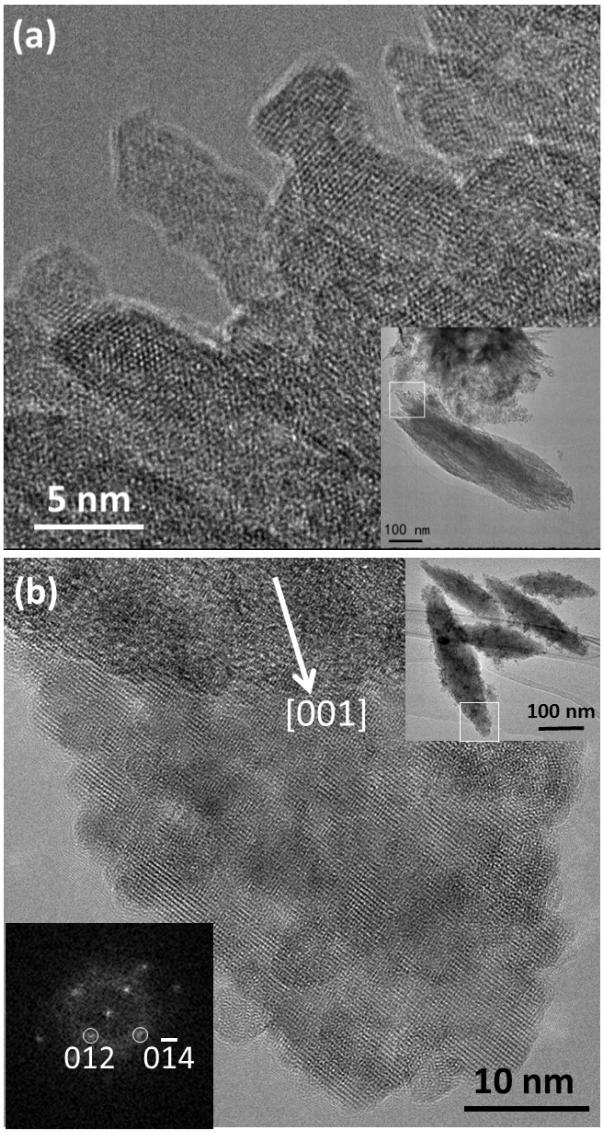

Figure 3. (a) HRTEM image of a spindle particle in LS220 after 50 min., showing parallel β-FeOOH nanorods. The inset is TEM image of the whole spindle particle with a square showing where the HRTEM image was recorded. (b) HRTEM image of LS220-1h showing a spindle particle with all the β-FeOOH nanorods decomposed to α-Fe_2O_3 nanocrystallites. The top inset is a TEM image of the whole particle with a square showing where the HRTEM was recorded. The bottom inset is the corresponding SAED pattern indexed to the α-Fe_2O_3 structure.

Step 5. The β-FeOOH nanorods in the spindle particles then decomposed into α-Fe_2O_3 nanocrystallites. This can be seen from the HRTEM image of Figure 3b. It is interesting to see that all the nanocrystallites are self-orientated and their [001] direction is parallel to the original [001] direction of β-FeOOH, *i.e.* also along the long axis of the spindle particle. Therefore, the corresponding SAED pattern looks like a single crystal pattern (bottom inset of Figure 3b). EDX of a spindle in sample LU220-1h shows characteristic X-ray peaks of O, P, and Fe without Cl as shown in SI, Figure S7. That means there are still a large amount of phosphate anions remained in the space between Fe_2O_3 nanocrystallites.

Although the crystal structures of β-FeOOH and α-Fe_2O_3 are quite different, one is tetragonal and another is rhombohedral, the phase transformation from the former to the latter can be achieved by atomic movements mainly on the (*ab*) planes. Figure 4 shows the crystal structures of (a) β-FeOOH and (b) α-Fe_2O_3, both viewing down the [001] zone axis. Two Fe layers along the **c** axis are included. On the (001) planes, the area of each unit cell of β-FeOOH is 108.99 Å^2. The structure can be constructed with four building units as highlighted by ovals in Figure 4a. A channel along the [001] direction is formed at the body-centered positions, which are large enough to house Cl^- anions to stabilize the structure.[29]

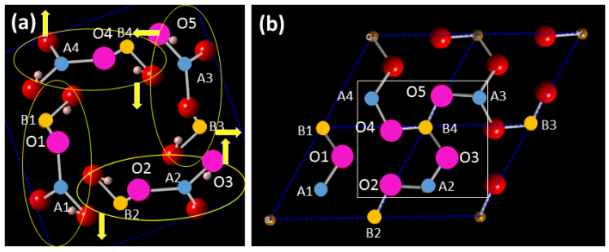

Figure 4. Schematic drawing of phase transformation from (a) β-FeOOH (one unit cell) to (b) α-Fe_2O_3 (2 x 2 unit cells), both on the [001] projection. The blue balls A1 to A4 represent Fe atoms in the same layer. The brown balls B1 to B4 represent Fe atoms in the next layer. The pink balls O1 to O5 represent O atoms. The small grey balls represent H atoms. The yellow ovals in (a) indicate the units which rotate and shift mainly on the (001) plane as indicated by the arrows towards the α-Fe_2O_3 structure.

The phase transformation from β-FeOOH to α-Fe_2O_3 can be achieved by rotating and shifting these units mainly in the (001) plane as indicated by yellow arrows in Figure 4a. While some H_2O molecules are released, not many other chemical bonds are broken. Eventually one square unit cell of β-FeOOH changes to 2 x 2 diamond unit cells of α-Fe_2O_3 as shown in Figure 4b. The area shrinks from 108.99 Å^2 to 87.92 Å^2. On the other hand, each unit cell of β-FeOOH along the [001] axis contains two Fe layers. Six such unit cells change to one unit cell of α-Fe_2O_3, containing 12 Fe layers. Consequently, 1 x 1 x 6 tetragonal superunit cell of β-FeOOH changes to 2 x 2 x 1 hexagonal unit cell of α-Fe_2O_3 with the [001] directions unchanged, both parallel to the long axis of the spindle in the samples under investigation. The corresponding volume changes from 1968.42 to 1224.04 Å^3, *i.e.* about 37.82% shrinkage. This significant volume shrinkage leads to a reduction of the particle size of the spindles during the phase transformation.

Step 6. With further hydrothermal treatment, the polycrystalline α-Fe_2O_3 spindle particles underwent surface recrystallization into a single crystal shell, forming a core-shell structure. The recrystallization extended from the surface to the core until all the Fe_2O_3 nanocrystallites were consumed. Hollow single crystals formed, while the rough particle surface gradually changed to a smooth surface.

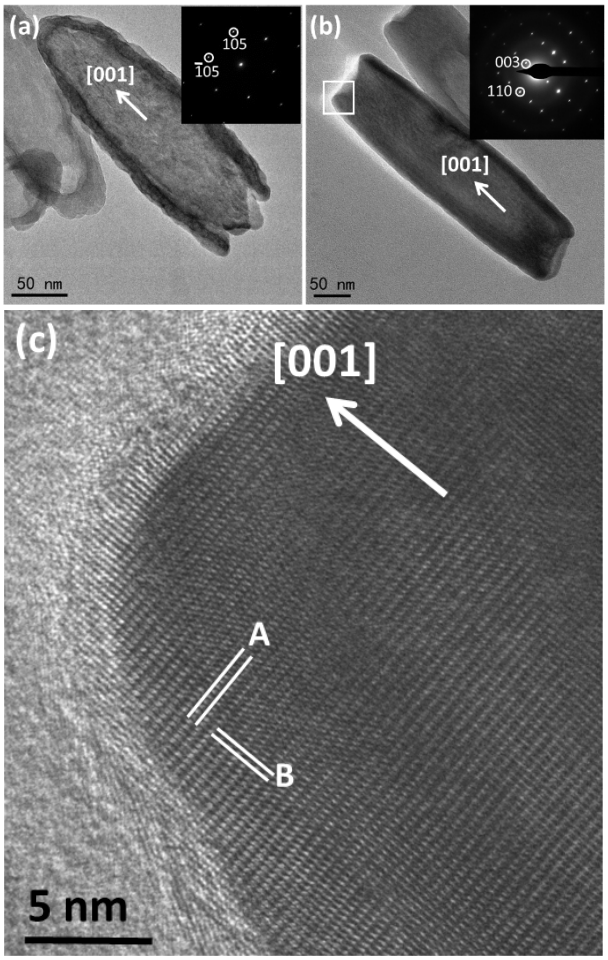

Figure 5. TEM images of (a) an one-end open nanotube in specimen LS220-48h and (b) a two-end open nanotube in LS220-120h. The insets are the corresponding SAED patterns, indexed to α-Fe_2O_3. (c) HRTEM taken from white rectangle area in (b). The d-spacings marked A and B are measured 4.61 Å and 2.53 Å, corresponding to the (003) and (110) planes of α-Fe_2O_3.

Step 7. The ends of the core-shell spindle particles, together with the core, were then dissolved, leading to the formation of nanotubes. In the weak acidic solution, (pH = 1.8 to 1.5 as measured in the beginning and at the end of reaction), the dissolution was very slow. It can be seen from the observation that no nanotubes formed at reaction temperature of 180 °C in several days. In the previous steps, phase transformation from β-FeOOH to α-Fe_2O_3, re-crystallization of α-Fe_2O_3 nanocrystallites into single crystalline shell dominated the process. The dissolution was not obvious even at 220 °C. A high concentration of the Fe^{3+} cations in the solution might inhibit the dissolution. When the growth of hematite stopped, the concentration of Fe^{3+} dropped to a minimum value, dissolution of the hematite shell in the core-shell spindles became notable. Since the (001) surface of α-Fe_2O_3 was the least protected surface plane by phosphate anions, the dissolution rate on that surface was much higher than on any other surfaces.[16] Consequently, the two ends of the spindle particles were dissolved, forming nanotubes (Figure 5a, 5b). The (003) diffraction spot in Figure 5b should be systematically absent according to the symmetry of the hematite structure. Its appearance is due to multiple scattering as also noticed by Zhang and his co-workers.[16]

As seen from the HRTEM image in Figure 5c, at the final stage, the whole nanotube particle has a single crystalline wall. This extension of re-crystallization inwards to the center of a particle is similar to the so-called reversed crystal growth mechanism, which was first established in 2007, and later was found in growth processes of many crystals, such as zeolites,[30,31] perovskite,[32] ZnO,[33] *etc*. and could be a common phenomenon which has been ignored for a long time.[34]

In the solution with the concentration of phosphate increased to 2.5 mM or 4.0 mM, the above mentioned steps 1, 2, and 3 were the same. However, the β-FeOOH nanorods did not aggregate into bundles in a parallel manner. The evolution of the material morphology followed another route as discussed below.

Step 4'. When the concentration of phosphate was high, a large amount of surface adsorbed phosphate anions made the nanorods surface more negatively charged. Therefore, the electrostatic repulsion made aggregation of the β-FeOOH nanorods difficult. Instead of forming parallel aggregation into spindle particles, the nanorods either stayed as individual particles or formed straw-like bundles, where nanorods repulsed each other at least at one end (see Figure S8 in SI). These straw-like particles were hardly seen in the low phosphate concentration system.

The individual β-FeOOH nanorods decomposed under the hydrothermal conditions into randomly orientated α-Fe_2O_3 nanocrystallites with an average size of 5 nm in diameter (Figure 6a). The nanorod morphology lost during this phase transformation. These nanocrystallites underwent self-orientated aggregation, mainly along the directions perpendicular to the [001] axis, to form some plates with crystal extension mainly on the (*ab*) plane. Although the nanocrystallites can still be identified in the image of the particles, SAED patterns show typical single crystal like patterns (Figure 6b). The plates stacked together face-to-face to form some nanodisks. Figure 6c is a TEM image showing some nanodisks with a top view (particle A) and a profile view (particles B). The nanoplates with obvious

gaps can only be observed with a profile view. All the nanocrystallites in such nanodisks are self-orientated, not only in the nanoplates but also in between the nanoplates, indicated by the lattice fringes in the HRTEM image (Figure 6d).

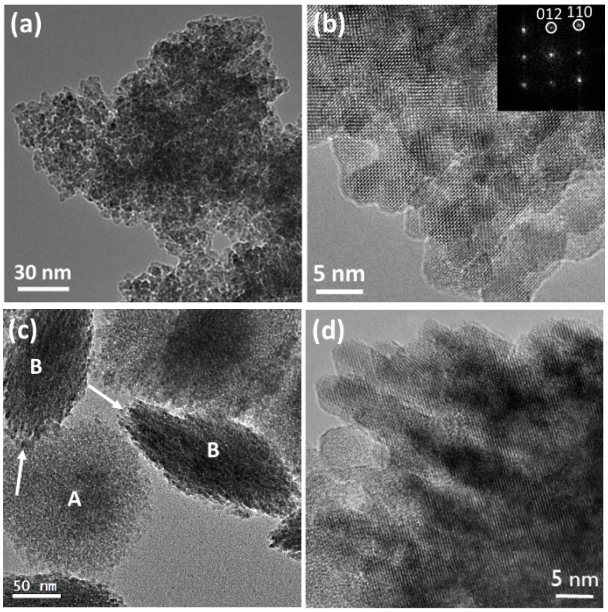

Figure 6. (a) TEM image of disordered and randomly orientated α-Fe_2O_3 nanocrystallites in HS220-2.5h. (b) HRTEM of HS220-2.75h, showing self-orientated α-Fe_2O_3 nanocrystallites. The inset is the corresponding SAED pattern indexed to α-Fe_2O_3. (c) TEM image of some nanodisks from HS220-3h. Particle A has a top view and particles B have a profile view of the disks. The arrows indicate stacking of nanoplates. (d) HRTEM image of the profile view of the nanoplates in a nanodisk.

It was noted that the formation of these α-Fe_2O_3 nanodisks was slow, which was not observed until the hydrothermal treatment at 220 °C for 2 h 45 min. Previous studies revealed that on the (001) plane of α-Fe_2O_3, all the surface hydroxyl groups were doubly coordinated to Fe^{3+}, leading to neutral sites, while (*hk*o) planes may contain either positively charged or negatively charged sites.[19,35] The interaction between the nanocrystallites was much stronger on the (*hk*o) planes. The relatively faster connection of the nanocrystallites on these planes led to the formation of nanoplates, which then stacked along the **c** axis into nanodisks, which had a size of around 150-180 nm in diameter and 63-85 nm in thickness.

Figure 7a shows a HRTEM image with a top view of a nanodisk. Although the nanocrystallites are still visible in the HRTEM image, their orientations are almost perfectly self-adjusted, allowing an intergrowth of the nanocrystallites to form a low-density or porous single crystal. The [001] axis is parallel to the short axis of the disks.

Step 5'. Similar to the spindle particles in the solution with a low phosphate concentration, surface re-crystallization also took place in the disks to create a shell with a high crystallinity. The edge of the nanodisks is thinner than the central part and underwent the fastest re-crystallization. Therefore, the crystallinity is higher and crystalline shell is thicker at the edge than at the faces.

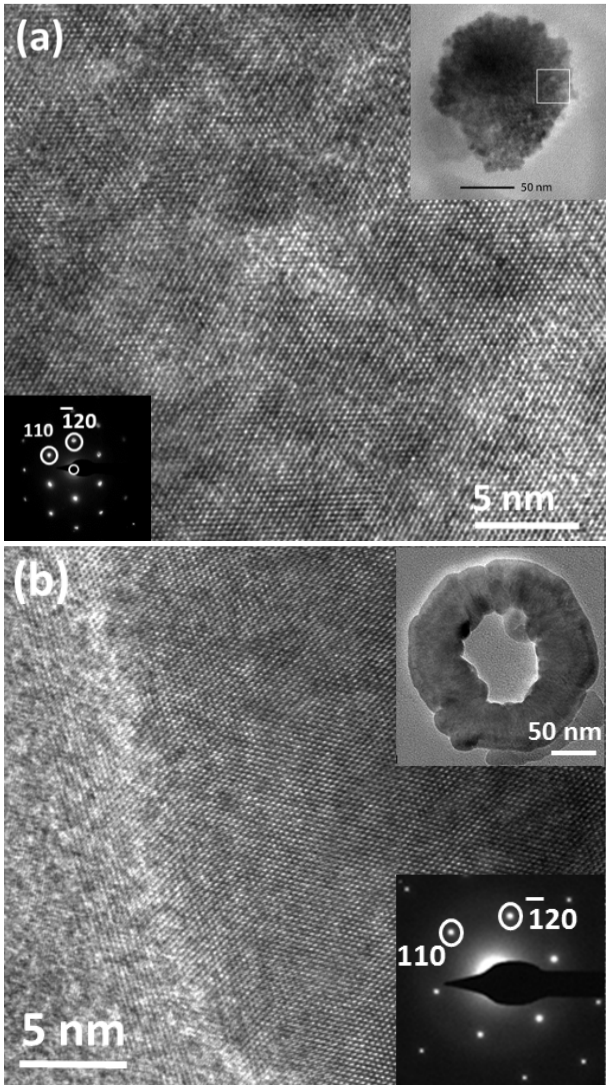

Figure 7. HRTEM images of (a) a nanodisk and (b) a nanoring with a view direction along the short axes of the particles. The top insets are TEM images showing the whole particles and the bottom insets are corresponding SAED patterns.

Step 6'. When the central area on both faces of a nanodisk was dissolved throughout the whole particle, a hole was made along the [001] direction and a nanoring appeared. Figure 7b shows a typical nanoring when viewing down its face, *i.e*. along the [001] axis of α-Fe_2O_3. The HRTEM image shows that it is single crystal.

In summary, based on the investigation mentioned above, we are able to reveal the formation mechanisms of

hematite nanotubes and nanorings, as depicted in Figure 8. In both the solutions with low and high concentrations of phosphate, polymerizations of phosphate and ferric chloride occurred (Figure 8a), followed by precipitation of these polymers into disordered particles (Figure 8b). β-FeOOH nanorods grew up in these particles (Figure 8c). These nanorods then underwent two different processes towards α-Fe_2O_3, depending on the phosphate concentration. In other words, the nanorods face a competition at this stage, either decompose directly into α-Fe_2O_3 nanocrystallites or aggregate side by side to form spindle-shaped particles before phase transformation to α-Fe_2O_3.

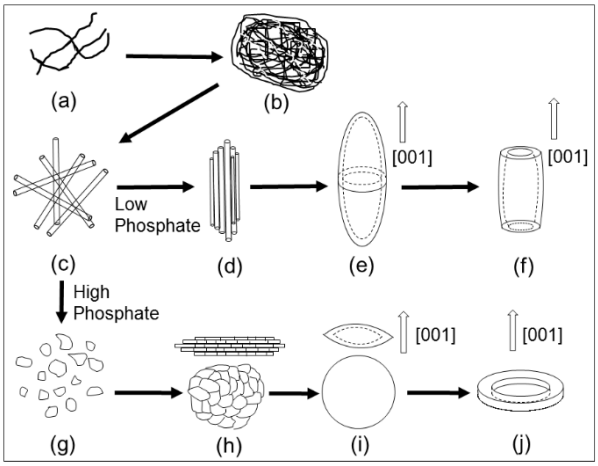

Figure 8. Formation Mechanisms of α-Fe_2O_3 nanotubes and nanorings via hydrolysis of $FeCl_3$ in the presence of phosphate. (a) Polymerization of precursor molecules/ions. (b) Formation of non-crystalline particles. (c) Growth of β-FeOOH nanorods. In the solution with a low concentration of phosphate, (d) formation of spindle particles. (e) Phase transformation to self-orientated α-Fe_2O_3 nanocrystallites, followed by formation of α-Fe_2O_3 shells. (f) Formation of nanotubes. In the solution with a high concentration of phosphate, (g) phase transformation to randomly oriented α-Fe_2O_3 nanocrystallites. (h) Oriented aggregation of α-Fe_2O_3 nanocrystallites into nanodisks. (i) Surface re-crystallization into single crystal shells. (j) Formation of nanorings.

In the case of a low concentration of phosphate, the interaction between the β-FeOOH nanorods was strong and they aggregated into spindle-shaped particles (Figure 8d). Phase transformation of β-FeOOH to self-orientated α-Fe_2O_3 nanocrystallites took place, while the spindle shape was maintained and the **c** axis of β-FeOOH directly changed to the **c** axis of α-Fe_2O_3, followed by surface re-crystallization into a single crystal shell (Figure 8e). In further hydrothermal treatment the ends and the cores of the spindle particles were dissolved, leading to the final product of α-Fe_2O_3 nanotubes (Figure 8f).

On the other hand, in the case of a high phosphate concentration, the individual β-FeOOH nanorods decomposed into randomly orientated α-Fe_2O_3 nanocrystallites (Figure 8g). The nanocrystallites selectively connected each other on the (*hko*) plane to form nanoplates, which stacked layer-by-layer to form nanodisks (Figure 8h). The surface of the nanodisks then underwent Ostwald ripening to form high crystallinity shells (Figure 8i). Hematite nanorings appeared when the nanodisks were partly eroded mainly in the central area until a hole was made (Figure 8j).

The measurement of the Fe^{3+} concentration in the liquid phase supports our proposed mechanisms. As shown by the inductively coupled plasma-optical emission spectrometry (ICP-OES) results of LS220 samples in Figure S9 in SI, in the first 2 hours, the concentration of Fe^{3+} drops down, because the Fe^{3+}-containing ions continuously precipitates. After 2 hours, the Fe^{3+} concentration keeps at a very low level. At this stage, chemical changes in the solid particles dominate. When the reaction time increases to 24 hours, the Fe^{3+} concentration increases, indicating the Fe_2O_3 particles are partially dissolved.

The perfect crystal orientations of the nanotubes and nanorings (see Figure 8f, 8j) resulted in that the major exposed surface on the nanorings is the (001) plane, while the surface of the nanotubes mainly terminated at the (*hko*) planes. To test if such a big difference might affect the surface related physico-chemical properties of the nanocrystals, their photoelectrochemical performance was examined.

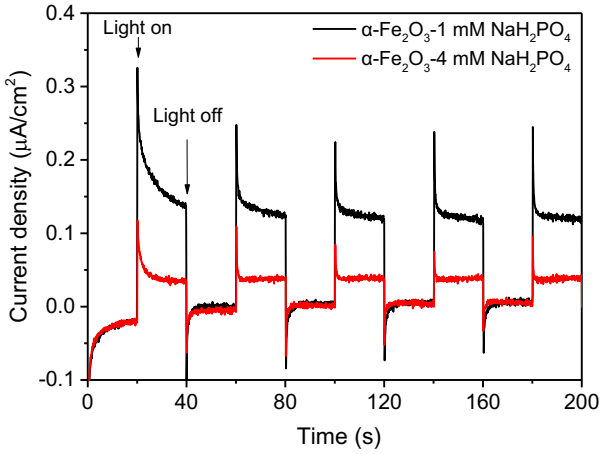

Figure 9. Current-time (I-t) curves of the α-Fe_2O_3 nanotubes and nanorings prepared in 1 mM and 4 mM NaH_2PO_4, respectively.

The current-time (I-t) curves of the α-Fe_2O_3 samples LS220-48h (nanotubes) and HS220-48h (nanorings) under visible light irradiation are shown in Figure 9. Obviously, the photocurrent increased sharply for both samples once the Xe lamp was switched on and the photocurrents decreased immediately once the Xe lamp was switched off. The sample of nanotubes displays about 3 times higher photocurrent responses than that of the sample of nanorings, indicating a higher photoelectrochemical water

splitting potential of the nanotubes. Moreover, the photocurrent spikes appeared when the light source was switched on or off.

Although the low band gap of hematite (2.2 eV) ensures a high efficiency of absorption of visible light, the ultrafast charge-hole recombination limits the actually generated photocurrent, which contributes to the oxidation of oxygen anions in water splitting. For example, a recent work using electron energy loss spectroscopy (EELS) attached to a 4D electron microscope indicated that the recombination of photogenerated Fe^{2+}-Fe^{4+} charge-hole pairs in hematite was in a scale of picosecond.[36] On the other hand, Sivula *et al*. found that the α-Fe_2O_3 specimen after annealing at 800 °C gave high transient photocurrent spikes. However, the samples annealing at 700 °C or below did not show such a property.[37] The high temperature annealing was speculated to induce lattice distortion, doping and increase crystal size. More importantly, the authors pointed out that the photocurrent might rely on the accumulation of photogenerated holes at the semiconductor liquid junction. In our photoelectrochemical test, the samples were not annealed. The transient photocurrent spikes were also observed, demonstrating an excellent charge separation efficiency, although the photocurrent is lower than quantum dots hematite photoanodes.[38] The different photocurrent values from nanotubes and nanorings are more likely attributed to their exposed surface planes, as the surface electronic structures on the (*hko*) and (001) planes are different, leading to different conductivities.

CONCLUSIONS

Single crystalline nanotubes and nanorings of α-Fe_2O_3 can be fabricated through hydrolysis of $FeCl_3$ in the presence of phosphate. However, the crystal growth is non-classical, *i.e*. each α-Fe_2O_3 crystal is not developed from a single nucleus, but from Ostwald ripening of nanocrystallites in spindle- and nanodisk-shaped polycrystalline particles. The α-Fe_2O_3 nanocrystallites do not form from single nuclei in the solution, but from decomposition of β-FeOOH nanorods. At an early stage when the β-FeOOH nanorods, as an intermediate phase, grow up, they face a competition between direct decomposition into disordered α-Fe_2O_3 nanocrystallites and aggregation in a parallel manner into spindle particles, which decompose later. Consequently, stability of the β-FeOOH crystals plays an important role in the formation of the different shapes of the hematite crystals, leading to different major exposed surface planes, (*hko*) in the nanotubes and (001) in the nanorings. The photocurrent generated from the nanotubes is 3 times higher than that from the nanorings, implying that the surface structures may play an important role in the photoelectrochemical properties of hematite crystals.

ASSOCIATED CONTENT

Supporting Information

The Supporting Information is available free of charge on the ACS Publications website at DOI:

Figure S1, XRD pattern of early stage α-Fe_2O_3. Figure S2, SEM images of LU220-1h, LU220-24h, LS220-1h, and LS220-24h. Figure S3, Mass spectra of polymerized precursor molecules. Figure S4, Mass spectrum and molecular model of polymerized phosphate. Figure S5, EDX of early stage precipitant particles. Figure S6, HRTEM image of β-FeOOH nanorods. Figure S7, EDX spectrum of a spindle particle in LU220-1h. Figure S8, TEM image of straw-like particles of β-FeOOH nanorods. Figure S9, Fe^{3+} concentration in the liquid phase of the LS220 samples after different reaction time.

AUTHOR INFORMATION

Corresponding Author

*E-mail: wzhou@st-andrews.ac.uk
ORCID
Wuzong Zhou: 0000-0001-9752-7076

Notes

The authors declare no competing financial interest.

ACKNOWLEDGMENT

JC thanks joint scholarship from Chinese Ministry of Education (CSC grant) and University of St Andrews. We thank the EPSRC for financial support on FEG-SEM equipment (EP/F019580/1) and Titan Themis S/TEM microscope (EP/L017008/01). The authors also thank Maria Nowosielska for her assistance in the ICP experiments.

REFERENCES

(1) Zhong, D. K.; Sun, J. W.; Inumaru, H.; Gamelin, D. R. Solar Water Oxidation by Composite Catalyst/α-Fe_2O_3 Photoanodes. *J. Am. Chem. Soc*. **2009**, *131*, 6086–6087.

(2) Nithya, V. D.; Sabari Arul, N. Review on α-Fe_2O_3 Based Negative Electrode for High Performance Supercapacitors. *J. Power Sources* **2016**, *327*, 297–318.

(3) Cornell, R. M.; Schwertmann, U. The Iron Oxides: Structure, Properties, Reactions, Occurrences and Uses. 2nd Ed. Wiley-VCH. **2003**.

(4) Xiang, Q. Y.; Cao, J. L.; Li, Y.; Huang, Y. L.; Shi, Y.; Wang, J.; Mo, L. B.; Yao, W. Q. A Green, Low-Cost and Efficient Photocatalyst: Atomic-Hydrogenated α-Fe_2O_3. *Catal. Surv. Asia* **2016**, *20*, 133–140.

(5) Sivula, K.; Formal, F. L.; Grätzel, M. Solar Water Splitting: Progress Using Hematite (α-Fe_2O_3) Photoelectrodes. *ChemSusChem* **2011**, *4*, 432–449.

(6) Yeh, L. R.; Hackerman, N. Iron Oxide Semiconductor Electrodes in Photoassisted Electrolysis of Water. *J. Electrochem. Soc*. **1977**, *124*, 833–836.

(7) Chan, J. Y.; Ang, S. Y.; Ye, E. Y.; Sullivan, M.; Zhang, J.; Lin, M. Heterogeneous Photo-Fenton Reaction on Hematite (α-Fe_2O_3) {104}, {113} and {001} Surface Facets. *Phys. Chem. Chem. Phys*. **2015**, *17*, 25333–25341.

(8) Du, P.; Song, L. X.; Xia, J.; Teng, Y.; Yang, Z. K. Construction and Application of α-Fe_2O_3 Nanocubes Dominated by the Composite Interaction between Polyvinyl Chloride and Potassium Ferrocyanide. *J. Mater. Chem. A*, **2014**, *2*, 11439–11447.

(9) Wang, C.; Wang, T. S.; Wang, B. Q. Zhou, X.; Cheng, X. Y.; Sun, P.; Zheng, J.; Lu, G. Y. Design of α-Fe_2O_3 Nanorods Functionalized Tubular NiO Nanostructure for Discriminating Toluene Molecules. *Sci. Rep*. **2016**, *6*, 26432.

(10) Saveh-Shemshaki, N.; Latifi, M.; Bagherzadeh, R.; Byranvand, M. M.; Naseri, N.; Dabirian, A. Synthesis of Mesoporous Functional Hematite Nanofibrous Photoanodes by Electrospinning. *Polym. Advan. Technol*. **2016**, *27*, 358–365.

(11) Tadic, M.; Kopanja, L.; Panjan, M.; Kralj, S.; Nikodinovic-Runic, J.; Stojanovic, Z. Synthesis of Core-shell Hematite (α-Fe_2O_3) Nanoplates: Quantitative Analysis of the Particle Structure and Shape, High Coercivity and Low Cytotoxicity. *Appl. Surf. Sci*. **2017**, *403*, 628–634.

(12) Yue, B.; Tang, H.; Kong, Z.; Zhu, K.; Dickinson, C.; Zhou, W. Z.; He, H. Y. Preparation and Characterisation of Three-dimensional Mesoporous Crystals of WO_3. *Chem. Phys. Lett*. **2005**, *407*, 83–86.

(13) Su, Z. X.; Dickinson, C.; Wan, Y. T.; Wang, Z. L.; Wang, Y. W.; Sha, J.; Zhou, W. Z. Crystal Growth of Si Nanowires and Formation of Longitudinal Planar Defects. *CrystEngComm* **2010**, *12*, 2793–2798.

(14) Reeves, N. J.; Mann, S. Influence of Inorganic and Organic Additives on the Tailored Synthesis of Iron Oxides. *J. Chem. Soc. Faraday Trans*. **1991**, *87*, 3875–3880.

(15) Kandori, K.; Ohnishi, S.; Fukusumi, M.; Morisada, Y. Effects of Anions on the Morphology and Structure of Hematite Particles Produced from Forced Hydrolysis of $Fe(NO_3)_3$-HNO_3. *Colloid Surface A*. **2008**, *331*, 232–238.

(16) Jia, C. J.; Sun, L. D.; Yan, Z. G.; You, L. P.; Luo, F.; Han, X. D.; Pang, Y. C.; Zhang, Z.; Yan, C. H. Single-Crystalline Iron Oxide Nanotubes. *Angew. Chem. Int. Ed*. **2005**, *44*, 4328–4333.

(17) Jia, C. J.; Sun, L. D.; Yan, Z. G.; Pang, Y. C.; You, L. P.; Yan, C. H. Iron Oxide Tube-in-Tube Nanostructures. *J. Phys. Chem. C*. **2007**, *111*, 13022–13027.

(18) Lv, B. L.; Xu, Y.; Wu, D.; Sun, Y. H. Morphology Evolution of α-Fe_2O_3 Nanoparticles: the Effect of Dihydrogen Phosphate Anions. *CrystEngComm* **2011**, *13*, 7293–7298.

(19) Liu, Z.; Chiang, C. Y.; Li, W.; Zhou, W. Z. The Role of Surface Hydrolysis of Ferricyanide Anions in Crystal Growth of Snowflake-shaped α-Fe_2O_3. *Chem. Commun*. **2015**, *51*, 9350–9353.

(20) Green, A. E.; Chiang, C. Y.; Greer, H. F.; Waller, A.; Ruszin, A.; Webster, J.; Niu, Z. Y.; Self, K.; Zhou, W. Z. Growth Mechanism of Dendritic Hematite via Hydrolysis of Ferricyanide. *Cryst. Growth Des*. **2017**, *17*, 800–808.

(21) Liu, Z.; Yu, R. T.; Dong, Y. P.; Li, W.; Zhou, W. Z. Preparation of α-Fe_2O_3 Hollow Spheres, Nanotubes, Nanoplates and Nanorings as Highly Efficient Cr(VI) Adsorbents. *RSC Adv*. **2016**, *6*, 82854–82861.

(22) Spiro, T. G.; Allerton, S. E.; Renner, J.; Terzis, A.; Bils, R.; Saltman, P. The Hydrolytic Polymerization of Iron(III). *J. Am. Chem. Soc*. **1966**, *88*, 2721–2726.

(23) FlynnJr, C. M. Hydrolysis of Inorganic Iron(III) Salts. *Chem. Rev*. **1984**, *84*, 31–41.

(24) Smith E. A.; Estroff L. A. Role of Akaganeite (β-FeOOH) in the Growth of Hematite (α-Fe_2O_3) in an Inorganic Silica Hydrogel. *Cryst. Growth Des*. **2015**, *15*, 3388–3398.

(25) Xavier A. M.; FerreiraF. F.; Souza F. L. Morphological and Structural Evolution from Akaganeite to Hematite of Nanorods Monitored by ex situ Synchrotron X-ray Powder Diffraction. *RSC Adv*. **2014**, *4*, 17753–17759.

(26) Chitrakar, R.; Tezuka, S.; Sonoda, A.; Sakane, K.; Ooi, K.; Hirotsu, T. Phosphate Adsorption on Synthetic Goethite and Akaganeite. *J. Colloid Interf. Sci*. **2006**, *298*, 602–608.

(27) Kim, J.; Li, W.; Philips, B. L.; Grey, C. P. Phosphate Adsorption on the Iron Oxyhydroxides Goethite (α-FeOOH), Akaganeite (β-FeOOH), and Lepidocrocite (γ-FeOOH): a ^{31}P NMR Study. *Energy Environ. Sci*. **2011**, *4*, 4298–4305.

(28) Borggaard, O. K. Effects of Surface Area and Mineralogy of Iron Oxides on Their Surface Charge and Anion-Adsorption Properties. *Clay. Clay Miner*. **1983**, *31*, 230–232.

(29) Ståhl, K.; Nielsen, K.; Jiang, J. Z.; Lebech, B.; Hanson, J. C.; Norby, P.; Lanschot, J. V. On the Akaganéite Crystal Structure, Phase Transformations and Possible Role in Post-excavational Corrosion of Iron Artifacts. *Corros. Sci*. **2003**, *45*, 2563–2575.

(30) Chen, X. Y.; Qiao, M. H.; Xie, S. H.; Fan, K. N.; Zhou, W. Z.; He, H. Y. Self-Construction of Core–Shell and Hollow Zeolite Analcime Icositetrahedra: A Reversed Crystal Growth Process via Oriented Aggregation of Nanocrystallites and Recrystallization from Surface to Core. *J. Am. Chem. Soc*. **2007**, *129*, 13305–13312.

(31) Yao, J. F.; Li, D.; Zhang, X. Y.; Kong, C. H.; Yue, W. B.; Zhou, W. Z.; Wang, H. T. Cubes of Zeolite A with an Amorphous Core. *Angew. Chem. Int. Ed*. **2008**, *47*, 8397–8399.

(32) Yang, X. F.; Fu, J. X.; Jin, C. J.; Liang, C. L.; Wu, M. M.; Zhou, W. Z. Formation Mechanism of $CaTiO_3$ Hollow Crystals with Different Microstructures, *J. Am. Chem. Soc*. **2010**, *132*, 14279–14287.

(33) Self, K.; Zhou, H. J.; Greer, H. F.; Tian, Z. R.; Zhou, W. Z. Reversed Crystal Growth of ZnO Microdisks. *Chem. Commun*. **2013**, *49*, 5411–5413.

(34) Zhou, W. Z. Reversed Crystal Growth: Implications for Crystal Engineering. *Adv. Mater*. **2010**, *22*, 3086–3092.

(35) Barrón, V.; Torrent, J. Surface Hydroxyl Configuration of Various Crystal Faces of Hematite and Goethite. *J. Colloid Interf. Sci*. **1996**, *177*, 407–410.

(36) Su, Z. X. ; Baskin, J. S. ; Zhou, W. Z. ; Thomas, J. M. ; Zewail, A. H. Ultrafast Elemental and Oxidation-state Mapping of Hematite by 4D Electron Microscopy. *J. Am. Chem. Soc*. **2017**, *139*, 4916–4922.

(37) Sivula, K.; Zboril, R.; Le Formal, F.; Robert, R.; Weidenkaff, A.; Tucek, J.; Frydrych, J.; Grätzel, M. *J. Am. Chem. Soc*. **2010**, *132*, 7436–7444.

(38) Hu, Z.; Shen, Z.; Yu, J. C.; Cheng, F. *Appl. Catal. B*: *Environ*. **2017**, *203*, 829–838.

For Table of Contents Use Only

Chemistry of Hydrolysis of $FeCl_3$ in the Presence of Phosphate to Form Hematite Nanotubes and Nanorings

Jialu Chen, Shona Macfarlane, Chenxi Zhang, Kai Yu, and Wuzong Zhou

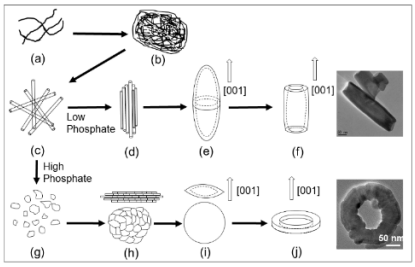

Through investigation of the intermediate specimens during the hydrolysis of $FeCl_3$ in the presence of phosphate, the formation mechanisms of α-Fe_2O_3 nanotubes and nanorings were revealed. The principal exposed surfaces (hko) in the nanotubes and (001) in the nanorings were understood.